SIAM J. SCI. COMPUT.
Vol. 35, No. 5, pp. A2188–A2206

INVERSE SOURCE PROBLEMS FOR THE HELMHOLTZ EQUATION AND THE WINDOWED FOURIER TRANSFORM II*

ROLAND GRIESMAIER†, MARTIN HANKE‡, AND THORSTEN RAASCH‡

Abstract. In this work we extend the qualitative reconstruction method for inverse source problems for time-harmonic acoustic and electromagnetic waves in free space, recently developed in [R. Griesmaier, M. Hanke, and T. Raasch, *SIAM J. Sci. Comput.*, 34 (2012), pp. A1544–A1562], to a relevant three-dimensional setting. The reconstruction algorithm relies on the fact that a windowed Fourier transform of the far field pattern of the wave radiated by a compactly supported source approximates an exponential ray transform with a purely imaginary exponent of a mollified version of the source. A filtered backprojection scheme for the standard ray transform applied to the absolute values of the windowed Fourier transform of the far field pattern is used to recover information on the support of the source. We provide the theoretical foundation of the method, discuss a numerical implementation of the fully three-dimensional algorithm, and present a series of numerical examples, including an inverse scattering problem, to support our theoretical results.

Key words. inverse source problem, Helmholtz equation, exponential ray transform, filtered backprojection, inverse Radon approximation

AMS subject classifications. 35R30, 65N21, 44A12

DOI. 10.1137/130908658

1. Introduction.

Inverse source problems for time-harmonic acoustic or electromagnetic waves consist in recovering information on unknown sources from observations of radiated waves away from the sources. These problems are well known to be severely ill-posed, but they also have important applications, such as, e.g., inverse scattering, where the aim is to deduce properties of an obstacle or of an inhomogeneous medium from near field or far field measurements of scattered waves. Inverse scattering can be treated as an inverse source problem, and this may, in fact, be the only reasonable approach if only one single incident wave is used and no a priori knowledge on physical and topological properties of the scatterers is available, because in this case alternative algorithms like, for example, nonlinear optimization techniques or linear sampling and factorization methods (see, e.g., Colton and Kress [5]), are not applicable.

Without further assumptions inverse source problems do not have a unique solution. Thus the classical approach is to consider least squares formulations and corresponding regularization schemes, or backpropagation algorithms (see, e.g., Devaney [6, sect. 5] and Devaney, Marengo, and Li [7]). Typically, the corresponding reconstructions exhibit artifacts due to the oscillatory nature of the associated point spread functions (compare [6, p. 220] for an illustration). Therefore a variety of alternative ideas has been developed, in particular for the special case of point sources (cf., e.g., [2, 4, 9, 10, 14]), where uniqueness holds (see Isakov [17]). For the general case of arbitrary compactly supported sources only few reconstruction methods are

*Submitted to the journal's Methods and Algorithms for Scientific Computing section February 5, 2013; accepted for publication (in revised form) June 27, 2013; published electronically September 10, 2013.
http://www.siam.org/journals/sisc/35-5/90865.html
†Mathematisches Institut, Universität Leipzig, 04009 Leipzig, Germany (griesmaier@math.uni-leipzig.de).
‡Institut für Mathematik, Johannes Gutenberg-Universität Mainz, 55099 Mainz, Germany (hanke@math.uni-mainz.de, raasch@uni-mainz.de).

available: Here we like to mention a very recent algorithm suggested by Kress and Rundell [18], albeit restricted to low frequencies, and a method by Ikehata [16] for the reconstruction of sources supported on polygonal domains.

In [19, 20] Kusiak and Sylvester established a generalized notion of solution for inverse source problems with compactly supported sources, namely, the convex scattering support, which is the smallest convex set carrying a source that radiates a wave that is compatible with the given data. Furthermore, Sylvester extended this concept to unions of well separated convex sets in [25]. A numerical algorithm to approximate the convex scattering support from observations of the radiated wave has been discussed in [20] (see also Potthast, Kusiak, and Sylvester [23]), but no such scheme is currently available for the aforementioned extension to unions of well separated convex sets.

As a first step in this direction we recently proposed in [12] a new reconstruction scheme for the inverse source problem for the Helmholtz equation in two space dimensions. This method consists of two steps: In the first step the given far field data is preprocessed with a windowed Fourier transform to generate what we call *meta data*; in the second step a standard filtered backprojection for the Radon transform is applied to these meta data to produce images of the unknown source. These images are blurry, in particular at low wave numbers close to the resonance region, but they do not contain oscillatory artifacts and they provide useful information about the number and the positions of individual source components, as long as these are sufficiently far apart from each other in terms of wavelengths. As discussed in section 5 of [12], the reconstructed source locations approximate (in general nonconvex and not necessarily connected) subsets of the convex scattering support of the given far field data. The insight gained from these images can, for instance, be utilized to split the far field into the individual far field patterns radiated by each of the well separated source components, and to compute the associated convex scattering supports as an instance of a union of well separated convex sets that carry a source that is compatible with the data; cf. [13].

Here we generalize the reconstruction method from [12] to the more relevant three-dimensional case. While the conception of this generalization is similar to the two-dimensional case from a global point of view there are a number of subtle modifications that have been necessary to achieve our goal. First, we had to change our setting of the windowed Fourier transform on the unit sphere and treat it as a transform on the tangent bundle of the sphere rather than on the sphere itself; numerically, this amounts to an additional extrapolation step. Second, the exponential Radon transform with purely imaginary exponent from the two-dimensional case had to be replaced by an exponential ray transform with purely imaginary exponent. The latter now also allows for a more straightforward extension of the reconstruction method to limited aperture data. Last but not least the numerical realization as well as the associated sampling considerations are considerably more involved. At this occasion we like to mention that windowed Fourier transform techniques have previously been applied by Bellizzi and Capozzoli [3] to three-dimensional near field data, but no connection to the exponential ray transform (or a similar integral transform) has been exploited in this work.

The outline of our paper is as follows. In section 2 we introduce the mathematical setting and recall some facts on the far field pattern radiated by a time-harmonic acoustic source. Then, in sections 3–5 we discuss the windowed Fourier transform of the far field on the sphere, and we establish a relation to the exponential ray transform of the associated source. In section 6 we motivate how this analysis can

be applied to imaging purposes, and we comment on its numerical implementation in section 7. Section 8 contains a series of numerical examples to illustrate potentials and limitations of this scheme, and we close with some concluding remarks.

2. Problem setting. To begin with, we specify notation that is used throughout this article. Boldface Latin letters $\boldsymbol{x}$, $\boldsymbol{y}$, $\boldsymbol{z}$ always refer to space variables in $\mathbb{R}^3$, while the boldface Greek letters $\boldsymbol{\xi}$ and $\boldsymbol{\eta}$ are reserved for the corresponding dual variables in the Fourier domain. Throughout $|\cdot|$ denotes the Euclidean norm on $\mathbb{R}^n$ or $\mathbb{C}^n$, $n = 1, 2, 3$, and the symbol $\cdot$ is used for the corresponding (bilinear) scalar product in $\mathbb{R}^n$.

The variable on the unit sphere $S^2 \subset \mathbb{R}^3$ will typically be denoted by $\boldsymbol{\theta}$, unless it is connected to a space vector that has been rescaled to have unit norm, in which case the variable inherits the name of the space variable augmented by a hat symbol to emphasize its role in S^2, e.g., $\widehat{\boldsymbol{x}} = \boldsymbol{x}/|\boldsymbol{x}|$.

Finally, the boldface Latin letter $\boldsymbol{p}$ is used to denote the variable on the tangent space $\mathcal{T}_{\boldsymbol{\theta}} S^2 \subset \mathbb{R}^3$ at some $\boldsymbol{\theta} \in S^2$; for brevity we denote this space by $\boldsymbol{\theta}^\perp$. We write $\boldsymbol{p} = \boldsymbol{x}'_{\boldsymbol{\theta}}$ for the projection of $\boldsymbol{x} \in \mathbb{R}^3$ onto $\boldsymbol{\theta}^\perp$. The corresponding dual variable of $\boldsymbol{p}$ in the Fourier domain is $\boldsymbol{\omega}$. At some occasions, though, we need to reinterpret $\boldsymbol{\omega}$ as space variable; we will do so with extra care and highlight such changes appropriately.

The (sesquilinear) inner product in $L^2(X)$ is denoted by $\langle \cdot, \cdot \rangle_X$, and the same symbol is used for its extension to distributions acting on $C_0^\infty(X)$, respectively, $C_0(X)$, i.e., the space of C^∞, respectively, continuous, functions with compact support. For simplicity we will restrict our attention to (complex valued) compactly supported distributions $f \in \mathcal{E}'(\mathbb{R}^3)$ of order zero with $\operatorname{supp}(f) \subset B_R(0)$, a ball of radius $R > 0$ around the origin, in which case f can be extended to a continuous functional on $C_0(\mathbb{R}^3)$ such that

$$|f(\phi)| \;\le\; C \sup_{B_R(0)} |\phi| \qquad \text{for all } \phi \in C_0(\mathbb{R}^3)$$

with a constant $C > 0$ independent of ϕ. The smallest admissible value of C is given by $\|f\|_{C_0'(\mathbb{R}^3)}$, i.e., the norm of the extension of f in the dual space of $C_0(\mathbb{R}^3)$.

Given such a compactly supported distribution f, the *radiating solution* of the source problem

$$-\Delta u - \kappa^2 u = f \qquad \text{in } \mathbb{R}^3\,,$$

i.e., the uniquely determined solution that satisfies the *Sommerfeld radiation condition*

$$\lim_{r\to\infty} r \left(\frac{\partial u}{\partial r} - \mathrm{i}\kappa u \right) = 0\,, \qquad r = |\boldsymbol{x}|\,,$$

can be written as a volume potential

$$u = \Phi_\kappa * f \qquad \text{in } \mathbb{R}^3\,, \tag{2.1}$$

where Φ_κ is the *fundamental solution* given by

$$\Phi_\kappa(\boldsymbol{x}) \;=\; \frac{e^{\mathrm{i}\kappa|\boldsymbol{x}|}}{4\pi|\boldsymbol{x}|}\,, \qquad \boldsymbol{x} \in \mathbb{R}^3\,,\ \boldsymbol{x} \neq 0\,.$$

For any $\boldsymbol{z} \in \mathbb{R}^3$ there holds

$$\Phi_\kappa(\boldsymbol{x} - \boldsymbol{z}) \;=\; \frac{e^{\mathrm{i}\kappa|\boldsymbol{x}|}}{4\pi|\boldsymbol{x}|} e^{-\mathrm{i}\kappa\widehat{\boldsymbol{x}}\cdot\boldsymbol{z}} + \mathcal{O}\big(|\boldsymbol{x}|^{-2}\big) \qquad \text{for } |\boldsymbol{x}| \to \infty\,, \tag{2.2}$$

uniformly in all directions $\widehat{\boldsymbol{x}} := \boldsymbol{x}/|\boldsymbol{x}| \in S^2$ (cf., e.g., [5, p. 21]). Substituting (2.2) into (2.1) yields

$$u(\boldsymbol{x}) = \frac{e^{\mathrm{i}\kappa|\boldsymbol{x}|}}{4\pi|\boldsymbol{x}|} u^\infty(\widehat{\boldsymbol{x}}) + \mathcal{O}\big(|\boldsymbol{x}|^{-2}\big) \qquad \text{for } |\boldsymbol{x}| \to \infty\,,$$

where the *far field pattern* u^∞ is given by

$$u^\infty(\widehat{\boldsymbol{x}}) = \widehat{f}(\kappa\widehat{\boldsymbol{x}})\,, \qquad \widehat{\boldsymbol{x}} \in S^2\,, \tag{2.3}$$

i.e., by the three-dimensional Fourier transform

$$\widehat{f}(\boldsymbol{\xi}) = \int_{\mathbb{R}^3} e^{-\mathrm{i}\boldsymbol{\xi}\cdot\boldsymbol{x}} f(\boldsymbol{x})\,\mathrm{d}\boldsymbol{x}\,, \qquad \boldsymbol{\xi} \in \mathbb{R}^3\,,$$

of f evaluated on the sphere of radius κ around the origin. In this case we say that u^∞ is radiated by the source f.

The inverse problem considered in this work is to recover properties of the support of the unknown source f from knowledge of the far field pattern u^∞. To this end it will occasionally be useful to consider the spherical harmonics expansion

$$u^\infty(\boldsymbol{\theta}) = \sum_{n=0}^{\infty} \sum_{m=-n}^{n} a_n^m Y_n^m(\boldsymbol{\theta})\,, \qquad \boldsymbol{\theta} \in S^2\,, \tag{2.4}$$

of the far field pattern, where

$$a_n^m = \int_{S^2} u^\infty(\boldsymbol{\theta})\overline{Y_n^m(\boldsymbol{\theta})}\,\mathrm{d}s(\boldsymbol{\theta}) = \int_{\mathbb{R}^3} f(\boldsymbol{x}) \overline{\int_{S^2} e^{\mathrm{i}\kappa\boldsymbol{\theta}\cdot\boldsymbol{x}} Y_n^m(\boldsymbol{\theta})\,\mathrm{d}s(\boldsymbol{\theta})}\,\mathrm{d}\boldsymbol{x}\,.$$

Applying the Funk–Hecke formula (see, e.g., [5, pp. 31–32]) the integral over S^2 can be evaluated explicitly to obtain

$$a_n^m = \frac{4\pi}{\mathrm{i}^n} \int_{\mathbb{R}^3} f(\boldsymbol{x}) j_n(\kappa|\boldsymbol{x}|)\overline{Y_n^m(\widehat{\boldsymbol{x}})}\,\mathrm{d}\boldsymbol{x}\,, \tag{2.5}$$

where j_n denote the spherical Bessel functions of order n, which are related to the standard Bessel functions by

$$j_n(\kappa|\boldsymbol{x}|) = \frac{\sqrt{\pi}}{\sqrt{2\kappa|\boldsymbol{x}|}}\, J_{n+1/2}(\kappa|\boldsymbol{x}|)\,, \qquad n \in \mathbb{N}$$

(see Abramowitz and Stegun [1, 10.1.1]). Since

$$j_n(\kappa|\boldsymbol{x}|) \sim \frac{1}{2\sqrt{\kappa|\boldsymbol{x}|}} \frac{1}{\sqrt{n+1/2}} \left(\frac{e\kappa|\boldsymbol{x}|}{2n+1}\right)^{n+1/2} \qquad \text{for } n \to \infty \tag{2.6}$$

(cf. [1, 9.3.1]), and as we have assumed that $\operatorname{supp} f \subset B_R(0)$, the spherical harmonics coefficients a_n^m decay superlinearly as a function of n for $n \gtrsim \kappa R$, and hence, are essentially supported in the range $n \lesssim \kappa R$.

3. Local analysis of the far field pattern. For a local analysis of the given far field pattern $u^\infty \in C^\infty(S^2)$ we take a (one-dimensional) Gaussian kernel

$$\chi_\varepsilon(t) = \frac{1}{\sqrt{2\pi\varepsilon^2}}\, e^{-\frac{1}{2}t^2/\varepsilon^2}\,, \qquad t \in \mathbb{R}\,, \tag{3.1}$$

with standard deviation ε, and define a windowed Fourier transform of the far field pattern u^∞ on the sphere by

$$(S_\varepsilon u^\infty)(\boldsymbol{\theta},\boldsymbol{\omega}) := \int_{\boldsymbol{\theta}^\perp} e^{-\mathrm{i}\boldsymbol{\omega}\cdot\boldsymbol{p}}\chi_\varepsilon(|\boldsymbol{p}|)u^\infty\left(\frac{\boldsymbol{\theta}+\boldsymbol{p}}{|\boldsymbol{\theta}+\boldsymbol{p}|}\right)\,\mathrm{d}s(\boldsymbol{p}) \tag{3.2}$$

for any $\boldsymbol{\theta}\in S^2$ and $\boldsymbol{\omega}\in\boldsymbol{\theta}^\perp$, where $\mathrm{d}s$ denotes the surface measure on $\boldsymbol{\theta}^\perp$. Other window functions are possible, but the derivation for the Gaussian is particularly simple, and this is the window that we have implemented anyway.

Remark 3.1. The windowed Fourier transform employed in (3.2) is conceptually different from the one we have used in [12] for the two-dimensional case, i.e., on S^1. There we applied the standard one-dimensional windowed Fourier transform directly to the angular variable of the unit circle. Given far field data on an equiangular grid this transform can be implemented with a one-dimensional FFT in a straightforward way.

In (3.2), on the other hand, we first project the far field data u^∞ to the tangent plane, and then compute the windowed Fourier transform in this plane. Using an equidistant grid on the tangent plane the latter can be implemented by means of a two-dimensional FFT, but the projection from the sphere requires additional efforts; see section 7. For the related discussion of an alternative windowed Fourier transform on the sphere we refer, e.g., to Torresani [26]. ◇

In order to analyze the windowed Fourier transform (3.2) we recall from (2.3) that

$$\begin{aligned} u^\infty\left(\frac{\boldsymbol{\theta}+\boldsymbol{p}}{|\boldsymbol{\theta}+\boldsymbol{p}|}\right) &= \int_{\mathbb{R}^3} e^{-\mathrm{i}\kappa\frac{\boldsymbol{\theta}+\boldsymbol{p}}{|\boldsymbol{\theta}+\boldsymbol{p}|}\cdot\boldsymbol{x}} f(\boldsymbol{x})\,\mathrm{d}\boldsymbol{x} \\ &= \int_{B_R(0)} e^{-\mathrm{i}\kappa(\boldsymbol{\theta}+\boldsymbol{p})\cdot\boldsymbol{x}}\, r(\boldsymbol{x};\boldsymbol{\theta},\boldsymbol{p}) f(\boldsymbol{x})\,\mathrm{d}\boldsymbol{x}\,, \end{aligned} \tag{3.3}$$

where

$$r(\boldsymbol{x};\boldsymbol{\theta},\boldsymbol{p}) := \exp\left(-\mathrm{i}\kappa\left(\frac{1}{|\boldsymbol{\theta}+\boldsymbol{p}|}-1\right)(\boldsymbol{\theta}+\boldsymbol{p})\cdot\boldsymbol{x}\right)$$

satisfies

$$\begin{aligned} \big|r(\boldsymbol{x};\boldsymbol{\theta},\boldsymbol{p})-1\big| &\le \left|\kappa\left(\frac{1}{|\boldsymbol{\theta}+\boldsymbol{p}|}-1\right)(\boldsymbol{\theta}+\boldsymbol{p})\cdot\boldsymbol{x}\right| \le \kappa|\boldsymbol{x}|\left(|\boldsymbol{\theta}+\boldsymbol{p}|-1\right) \\ &= \kappa|\boldsymbol{x}|\,\frac{|\boldsymbol{\theta}+\boldsymbol{p}|^2-1}{|\boldsymbol{\theta}+\boldsymbol{p}|+1} \le \kappa|\boldsymbol{x}|\,\frac{|\boldsymbol{p}|^2}{|\boldsymbol{\theta}+\boldsymbol{p}|+1} \le \frac{1}{2}\,\kappa|\boldsymbol{x}||\boldsymbol{p}|^2\,. \end{aligned} \tag{3.4}$$

In the derivation of (3.4) we have used that $|e^{\mathrm{i}\alpha}-1|\le|\alpha|$ for $\alpha\in\mathbb{R}$.

Inserting (3.3) into (3.2) we obtain

$$\begin{aligned} (S_\varepsilon u^\infty)(\boldsymbol{\theta},\boldsymbol{\omega}) &= \int_{\boldsymbol{\theta}^\perp} e^{-\mathrm{i}\boldsymbol{\omega}\cdot\boldsymbol{p}}\chi_\varepsilon(|\boldsymbol{p}|)\int_{B_R(0)} e^{-\mathrm{i}\kappa(\boldsymbol{\theta}+\boldsymbol{p})\cdot\boldsymbol{x}}\, r(\boldsymbol{x}) f(\boldsymbol{x})\,\mathrm{d}\boldsymbol{x}\,\mathrm{d}s(\boldsymbol{p}) \\ &= \delta + \int_{\boldsymbol{\theta}^\perp} e^{-\mathrm{i}\boldsymbol{\omega}\cdot\boldsymbol{p}}\chi_\varepsilon(|\boldsymbol{p}|)\int_{B_R(0)} e^{-\mathrm{i}\kappa(\boldsymbol{\theta}+\boldsymbol{p})\cdot\boldsymbol{x}} f(\boldsymbol{x})\,\mathrm{d}\boldsymbol{x}\,\mathrm{d}s(\boldsymbol{p}) \\ &= \delta + \int_{B_R(0)} e^{-\mathrm{i}\kappa\boldsymbol{\theta}\cdot\boldsymbol{x}} f(\boldsymbol{x})\int_{\boldsymbol{\theta}^\perp} e^{-\mathrm{i}(\boldsymbol{\omega}+\kappa\boldsymbol{x}'_{\boldsymbol{\theta}})\cdot\boldsymbol{p}}\chi_\varepsilon(|\boldsymbol{p}|)\,\mathrm{d}s(\boldsymbol{p})\,\mathrm{d}\boldsymbol{x} \\ &= \delta + \sqrt{2\pi\varepsilon^2}\int_{\mathbb{R}^3} e^{-\mathrm{i}\kappa\boldsymbol{\theta}\cdot\boldsymbol{x}} f(\boldsymbol{x})\,\widehat{\chi}_\varepsilon(|\boldsymbol{\omega}+\kappa\boldsymbol{x}'_{\boldsymbol{\theta}}|)\,\mathrm{d}\boldsymbol{x}\,, \end{aligned}$$

where $\widehat{\chi}_\varepsilon$ is the one-dimensional Fourier transform of χ_ε. The remainder term

$$\delta \;=\; \int_{B_R(0)} \left(\int_{\boldsymbol{\theta}^\perp} e^{-\mathrm{i}\boldsymbol{\omega}\cdot\boldsymbol{p}} \chi_\varepsilon(|\boldsymbol{p}|) e^{-\mathrm{i}\kappa(\boldsymbol{\theta}+\boldsymbol{p})\cdot\boldsymbol{x}} \big(r(\boldsymbol{x},\boldsymbol{p}) - 1\big) \,\mathrm{d}s(\boldsymbol{p}) \right) f(\boldsymbol{x}) \,\mathrm{d}\boldsymbol{x}$$

can be estimated with the help of (3.4) as

$$\begin{aligned} |\delta| \;&\le\; \frac{1}{2}\,|f|_{C_0'(\mathbb{R}^3)} \left(\kappa R \int_{\boldsymbol{\theta}^\perp} \chi_\varepsilon(|\boldsymbol{p}|) |\boldsymbol{p}|^2 \,\mathrm{d}s(\boldsymbol{p}) \right) \;=\; \pi\kappa R |f|_{C_0'(\mathbb{R}^3)} \int_0^\infty \chi_\varepsilon(t) t^3 \,\mathrm{d}t \\ &=\; \sqrt{2\pi}\,\kappa R |f|_{C_0'(\mathbb{R}^3)}\, \varepsilon^3 \end{aligned} \tag{3.5}$$

(cf. Gradshteyn and Ryzhik [11, 3.326]), which finally yields the representation

$$(S_\varepsilon u^\infty)(\boldsymbol{\theta},\boldsymbol{\omega}) \;=\; \sqrt{2\pi\varepsilon^2} \int_{\mathbb{R}^3} e^{-\mathrm{i}\kappa\boldsymbol{\theta}\cdot\boldsymbol{x}} f(\boldsymbol{x})\, \widehat{\chi}_\varepsilon(|\boldsymbol{\omega}+\kappa\boldsymbol{x}'_{\boldsymbol{\theta}}|) \,\mathrm{d}\boldsymbol{x} + \mathcal{O}\big(\kappa R |f|_{C_0'(\mathbb{R}^3)}\, \varepsilon^3\big)\,. \tag{3.6}$$

4. The exponential ray transform. To rewrite the right hand side of (3.6) in a more accessible form, we first define the *exponential ray transform* $P_{\mathrm{i}\kappa} : C_0^\infty(\mathbb{R}^3) \to C_0^\infty(T^2)$,

$$(P_{\mathrm{i}\kappa} g)(\boldsymbol{\theta},\boldsymbol{p}) \;:=\; \int_{\mathbb{R}} e^{\mathrm{i}\kappa t} g(\boldsymbol{p}+t\boldsymbol{\theta}) \,\mathrm{d}t\,,$$

where $T^2 = \{(\boldsymbol{\theta},\boldsymbol{p}) \mid \boldsymbol{\theta} \in S^2,\, \boldsymbol{p} \in \boldsymbol{\theta}^\perp\}$ denotes the tangent bundle on S^2. This is a special case of the attenuated ray transform with complex-valued attenuation (see, e.g., Natterer and Wübbeling [22, p. 27]), which for $\kappa = 0$ reduces to the standard ray transform (cf. [22, p. 17]). The backprojection operator $P_{\mathrm{i}\kappa}^* : C^\infty(T^2) \to C^\infty(\mathbb{R}^3)$ of the exponential ray transform given by

$$(P_{\mathrm{i}\kappa}^* h)(\boldsymbol{x}) \;=\; \int_{S^2} e^{-\mathrm{i}\kappa\boldsymbol{\theta}\cdot\boldsymbol{x}} h(\boldsymbol{\theta}, \boldsymbol{x}'_{\boldsymbol{\theta}}) \,\mathrm{d}s(\boldsymbol{\theta}) \tag{4.1}$$

satisfies

$$\langle P_{\mathrm{i}\kappa} g, h\rangle_{T^2} = \langle g, P_{\mathrm{i}\kappa}^* h\rangle_{\mathbb{R}^3} \qquad \text{for all } g \in C_0^\infty(\mathbb{R}^3) \text{ and } h \in C^\infty(T^2)\,. \tag{4.2}$$

Therewith, the exponential ray transform can be extended to $P_{\mathrm{i}\kappa} : \mathcal{E}'(\mathbb{R}^3) \to \mathcal{E}'(T^2)$ by duality (cf. Helgason [15, p. 32]). In the following lemma we collect some properties of this extension that will subsequently be used in section 5 below and that we have not been able to find in the literature.

LEMMA 4.1.

(a) *For any rapidly decreasing function $f \in \mathscr{S}(\mathbb{R}^3)$ we have*

$$\widehat{(P_{\mathrm{i}\kappa} f)}(\boldsymbol{\theta},\boldsymbol{\omega}) \;=\; \widehat{f}(\boldsymbol{\omega} - \kappa\boldsymbol{\theta}) \qquad \textit{for all } \boldsymbol{\theta} \in S^2 \textit{ and } \boldsymbol{\omega} \in \boldsymbol{\theta}^\perp\,,$$

where the Fourier transform of $P_{\mathrm{i}\kappa} f$ acts on the second variable $\boldsymbol{\omega} \in \boldsymbol{\theta}^\perp$.

(b) *For $f \in \mathcal{E}'(\mathbb{R}^3)$ and $g \in \mathscr{S}(\mathbb{R}^3)$ we have*

$$P_{\mathrm{i}\kappa}(f * g) = (P_{\mathrm{i}\kappa} f) * (P_{\mathrm{i}\kappa} g)\,. \tag{4.3}$$

Here the convolution on the right-hand side is with respect to the second variable of the tangent bundle T^2.

(c) *For the rescaled three-dimensional Gaussian*

$$g_{\varepsilon\kappa}(\boldsymbol{x}) := \varepsilon^2\kappa e^{1/(2\varepsilon^2)} e^{-\frac{1}{2}|\boldsymbol{x}|^2\varepsilon^2\kappa^2}, \qquad \boldsymbol{x}\in\mathbb{R}^3, \tag{4.4}$$

there holds

$$\psi_{\varepsilon\kappa}(\boldsymbol{p}) := (P_{\mathrm{i}\kappa} g_{\varepsilon\kappa})(\boldsymbol{\theta},\boldsymbol{p}) = \sqrt{2\pi\varepsilon^2}\, e^{-\frac{1}{2}|\boldsymbol{p}|^2\varepsilon^2\kappa^2}, \qquad \boldsymbol{\theta}\in S^2,\ \boldsymbol{p}\in\boldsymbol{\theta}^\perp, \tag{4.5}$$

which is the restriction to $\boldsymbol{\theta}^\perp$ of a (rescaled) Gaussian with the same covariance matrix.

Proof.

(a) Given $f\in\mathscr{S}(\mathbb{R}^3)$, $\boldsymbol{\theta}\in S^2$, and $\boldsymbol{\omega}\in\boldsymbol{\theta}^\perp$ we find that

$$\begin{aligned}(\widehat{P_{\mathrm{i}\kappa} f})(\boldsymbol{\theta},\boldsymbol{\omega}) &= \int_{\theta^\perp} e^{-\mathrm{i}\boldsymbol{\omega}\cdot\boldsymbol{p}} (P_{\mathrm{i}\kappa} f)(\boldsymbol{\theta},\boldsymbol{p})\,\mathrm{d}s(\boldsymbol{p})\\ &= \int_{\theta^\perp} e^{-\mathrm{i}\boldsymbol{\omega}\cdot\boldsymbol{p}} \int_{\mathbb{R}} e^{\mathrm{i}\kappa t} f(\boldsymbol{p}+t\boldsymbol{\theta})\,\mathrm{d}t\,\mathrm{d}s(\boldsymbol{p})\\ &= \int_{\mathbb{R}^3} e^{-\mathrm{i}(\boldsymbol{\omega}\cdot\boldsymbol{x}-\kappa\boldsymbol{\theta}\cdot\boldsymbol{x})} f(\boldsymbol{x})\,\mathrm{d}\boldsymbol{x} = \widehat{f}(\boldsymbol{\omega}-\kappa\boldsymbol{\theta}).\end{aligned}$$

(b) Given $f\in\mathcal{E}'(\mathbb{R}^3)$ and $g\in\mathscr{S}(\mathbb{R}^3)$, we first approximate f by a sequence $(f_n)_{n\in\mathbb{N}}\subset C_0^\infty(\mathbb{R}^3)$. Then, by part (a),

$$\begin{aligned}(P_{\mathrm{i}\kappa}(f_n * g))^\wedge(\boldsymbol{\theta},\boldsymbol{\omega}) &= (\widehat{f_n * g})(\boldsymbol{\omega}-\kappa\boldsymbol{\theta}) = \widehat{f_n}(\boldsymbol{\omega}-\kappa\boldsymbol{\theta})\,\widehat{g}(\boldsymbol{\omega}-\kappa\boldsymbol{\theta})\\ &= (\widehat{P_{\mathrm{i}\kappa} f_n})(\boldsymbol{\theta},\boldsymbol{\omega})\,(\widehat{P_{\mathrm{i}\kappa} g})(\boldsymbol{\theta},\boldsymbol{\omega}) = \big((P_{\mathrm{i}\kappa} f_n) * (P_{\mathrm{i}\kappa} g)\big)^\wedge(\boldsymbol{\theta},\boldsymbol{\omega}),\end{aligned}$$

which proves (4.3) for smooth functions. Thus, recalling (4.2) we find for all $h\in C^\infty(T^2)$ that

$$\begin{aligned}&\big\langle f_n * g, P_{\mathrm{i}\kappa}^* h\big\rangle_{\mathbb{R}^3}\\ &\quad= \langle P_{\mathrm{i}\kappa}(f_n * g), h\rangle_{T^2} = \langle (P_{\mathrm{i}\kappa} f_n) * (P_{\mathrm{i}\kappa} g), h\rangle_{T^2}\\ &\quad= \int_{S^2}\int_{\boldsymbol{\theta}^\perp}\int_{\boldsymbol{\theta}^\perp} P_{\mathrm{i}\kappa} f_n(\boldsymbol{\theta},\boldsymbol{\eta}-\boldsymbol{\omega}) P_{\mathrm{i}\kappa} g(\boldsymbol{\theta},\boldsymbol{\omega})\,\mathrm{d}s(\boldsymbol{\omega})\ \overline{h(\boldsymbol{\theta},\boldsymbol{\eta})}\,\mathrm{d}s(\boldsymbol{\eta})\ \mathrm{d}s(\boldsymbol{\theta})\\ &\quad= \int_{S^2}\int_{\boldsymbol{\theta}^\perp} P_{\mathrm{i}\kappa} f_n(\boldsymbol{\theta},\boldsymbol{\eta}) \left(\int_{\boldsymbol{\theta}^\perp} P_{\mathrm{i}\kappa} g(\boldsymbol{\theta},\boldsymbol{\omega})\overline{h(\boldsymbol{\theta},\boldsymbol{\omega}+\boldsymbol{\eta})}\,\mathrm{d}s(\boldsymbol{\omega})\right)\mathrm{d}s(\boldsymbol{\eta})\ \mathrm{d}s(\boldsymbol{\theta})\\ &\quad= \Big\langle P_{\mathrm{i}\kappa} f_n, \overline{\langle (P_{\mathrm{i}\kappa} g)(\boldsymbol{\theta},\cdot), h(\boldsymbol{\theta},\cdot+\boldsymbol{\eta})\rangle_{\boldsymbol{\theta}^\perp}}\Big\rangle_{T^2}\\ &\quad= \Big\langle f_n, P_{\mathrm{i}\kappa}^*\overline{\Big(\langle (P_{\mathrm{i}\kappa} g)(\boldsymbol{\theta},\cdot), h(\boldsymbol{\theta},\cdot+\boldsymbol{\eta})\rangle_{\boldsymbol{\theta}^\perp}\Big)}\Big\rangle_{\mathbb{R}^3}.\end{aligned}$$

Passing to the limit $n\to\infty$ this yields

$$\begin{aligned}&\big\langle P_{\mathrm{i}\kappa}(f * g), h\big\rangle_{T^2}\\ &\quad= \big\langle f * g, P_{\mathrm{i}\kappa}^* h\big\rangle_{\mathbb{R}^3} = \Big\langle f, P_{\mathrm{i}\kappa}^*\overline{\Big(\langle (P_{\mathrm{i}\kappa} g)(\boldsymbol{\theta},\cdot), h(\boldsymbol{\theta},\cdot+\boldsymbol{\eta})\rangle_{\boldsymbol{\theta}^\perp}\Big)}\Big\rangle_{\mathbb{R}^3}\\ &\quad= \Big\langle P_{\mathrm{i}\kappa} f, \overline{\langle (P_{\mathrm{i}\kappa} g)(\boldsymbol{\theta},\cdot), h(\boldsymbol{\theta},\cdot+\boldsymbol{\eta})\rangle_{\boldsymbol{\theta}^\perp}}\Big\rangle_{T^2}\\ &\quad= \int_{S^2}\big\langle (P_{\mathrm{i}\kappa} f)(\boldsymbol{\theta},\boldsymbol{\omega})(P_{\mathrm{i}\kappa} g)(\boldsymbol{\theta},\boldsymbol{\eta}), h(\boldsymbol{\theta},\boldsymbol{\omega}+\boldsymbol{\eta})\big\rangle_{\boldsymbol{\theta}^\perp\times\boldsymbol{\theta}^\perp}\,\mathrm{d}s(\boldsymbol{\theta})\\ &\quad= \big\langle (P_{\mathrm{i}\kappa} f) * (P_{\mathrm{i}\kappa} g), h\big\rangle_{T^2},\end{aligned}$$

which shows that (4.3) holds true for all $f\in\mathcal{E}'(\mathbb{R}^3)$ and $g\in\mathscr{S}(\mathbb{R}^3)$.

(c) For $\boldsymbol{\theta} \in S^2$ and $\boldsymbol{p} \in \boldsymbol{\theta}^\perp$ we finally compute

$$\begin{aligned}(P_{\mathrm{i}\kappa} g_{\varepsilon\kappa})(\boldsymbol{\theta}, \boldsymbol{p}) &= \int_{\mathbb{R}} e^{\mathrm{i}\kappa t} g_{\varepsilon\kappa}(\boldsymbol{p} + t\boldsymbol{\theta}) \, \mathrm{d}t \\ &= \varepsilon^2 \kappa \, e^{1/(2\varepsilon^2)} \int_{\mathbb{R}} e^{\mathrm{i}\kappa t} e^{-\frac{1}{2}(|\boldsymbol{p}|^2 + t^2)\varepsilon^2 \kappa^2} \, \mathrm{d}t \\ &= \varepsilon^2 \kappa \, e^{1/(2\varepsilon^2)} e^{-\frac{1}{2}|\boldsymbol{p}|^2 \varepsilon^2 \kappa^2} \int_{\mathbb{R}} e^{-\frac{1}{2} t^2 \varepsilon^2 \kappa^2 + \mathrm{i}\kappa t} \, \mathrm{d}t \\ &= \sqrt{2\pi} \, \varepsilon e^{-\frac{1}{2}|\boldsymbol{p}|^2 \varepsilon^2 \kappa^2} = \psi_{\varepsilon\kappa}(\boldsymbol{p}) \,. \qquad \square\end{aligned}$$

5. The connection to the windowed Fourier transform of the far field. We now formulate our main theoretical result, which connects the windowed Fourier transform of the far field with the exponential ray transform of the source.

THEOREM 5.1. *For the window χ_ε of* (3.1) *the windowed Fourier transform of the far field pattern u^∞ fulfills*

$$(S_\varepsilon u^\infty)(\boldsymbol{\theta}, \boldsymbol{\omega}) = \big(P_{\mathrm{i}\kappa}(g_{\varepsilon\kappa} * f)\big)\Big(-\boldsymbol{\theta}, -\frac{\boldsymbol{\omega}}{\kappa}\Big) + \mathcal{O}\big(\kappa R |f|_{C_0'(\mathbb{R}^3)} \, \varepsilon^3\big) \tag{5.1}$$

for $\boldsymbol{\theta} \in S^2$ and $\boldsymbol{\omega} \in \boldsymbol{\theta}^\perp$, where the Gaussian convolution kernel $g_{\varepsilon\kappa}$ is given by (4.4)*, and the unspecified constant of the remainder estimate can be bounded by $\sqrt{2\pi}$.*

Proof. Let $\boldsymbol{\theta} \in S^2$, $\boldsymbol{\omega} \in \boldsymbol{\theta}^\perp$, and $(f_n)_{n\in\mathbb{N}} \subset C_0^\infty(\mathbb{R}^3)$ be a sequence of smooth functions with compact support approximating f. Then, when substituting $\boldsymbol{x} = \boldsymbol{p} - t\boldsymbol{\theta}$ with $t \in \mathbb{R}$ and $\boldsymbol{p} \in \boldsymbol{\theta}^\perp$, we obtain for any $n \in \mathbb{N}$ that

$$\begin{aligned}\int_{\mathbb{R}^3} e^{-\mathrm{i}\kappa\boldsymbol{\theta}\cdot\boldsymbol{x}} f_n(\boldsymbol{x}) \, \widehat{\chi}_\varepsilon(|\boldsymbol{\omega} + \kappa \boldsymbol{x}'_{\boldsymbol{\theta}}|) \, \mathrm{d}\boldsymbol{x} &= \int_{\boldsymbol{\theta}^\perp} \widehat{\chi}_\varepsilon(|\boldsymbol{\omega} + \kappa\boldsymbol{p}|) \int_{\mathbb{R}} e^{\mathrm{i}\kappa t} f_n(\boldsymbol{p} - t\boldsymbol{\theta}) \, \mathrm{d}t \, \mathrm{d}s(\boldsymbol{p}) \\ &= \int_{\boldsymbol{\theta}^\perp} \widehat{\chi}_{\varepsilon\kappa}\Big(\big|\frac{\boldsymbol{\omega}}{\kappa} + \boldsymbol{p}\big|\Big) \, (P_{\mathrm{i}\kappa} f_n)(-\boldsymbol{\theta}, \boldsymbol{p}) \, \mathrm{d}s(\boldsymbol{p}) \,.\end{aligned}$$

Note that

$$\widehat{\chi}_{\varepsilon\kappa}(|\boldsymbol{z}|) = \frac{1}{\sqrt{2\pi\varepsilon^2}} \, \psi_{\varepsilon\kappa}(-\boldsymbol{z}) \qquad \text{for every } \boldsymbol{z} \in \mathbb{R}^3 \,,$$

where $\psi_{\varepsilon\kappa}$ has been defined in (4.5), so that the final integral times $\sqrt{2\pi\varepsilon^2}$ is a convolution of $\psi_{\varepsilon\kappa}$ and the exponential ray transform of f_n (with respect to the second variable $\boldsymbol{p} \in \boldsymbol{\theta}^\perp$). Therefore, letting $n \to \infty$ and f_n approximate f, it follows from (3.6) that

$$(S_\varepsilon u^\infty)(\boldsymbol{\theta}, \boldsymbol{\omega}) = \big(\psi_{\varepsilon\kappa} * (P_{\mathrm{i}\kappa} f)\big)\Big(-\boldsymbol{\theta}, -\frac{\boldsymbol{\omega}}{\kappa}\Big) + \mathcal{O}\big(\kappa R |f|_{C_0'(\mathbb{R}^3)} \, \varepsilon^3\big) \,, \tag{5.2}$$

where the remainder term δ is estimated explicitly in (3.5). By Lemma 4.1(c) the Gaussian $\psi_{\varepsilon\kappa}$ is the exponential ray transform of another Gaussian, namely, $g_{\varepsilon\kappa}$, and hence, the assertion (5.1) follows from the convolution property (4.3) of the exponential ray transform. $\square$

This result shows that with the Gaussian window function χ_ε of (3.1) the windowed Fourier transform $S_\varepsilon u^\infty$ of the far field pattern radiated by the source f can be considered a rescaled and rotated approximation of the exponential ray transform of the Gaussian mollification $g_{\varepsilon\kappa} * f$ of f. Note that in (5.1) we reinterpret the dual variable $\boldsymbol{\omega}$ as a space variable in the ray transform, and vice versa.

Remark 5.2. It is important to note that a smaller standard deviation ε of χ_ε not only leads to a smaller remainder term in (5.1), but also to a smaller essential band width of the corresponding mollifier $g_{\varepsilon\kappa}$ from (4.4). Therefore one has to balance the quality of the approximation (5.1) with the resolution of reconstructions to be obtained from $S_\varepsilon u^\infty$. $\diamond$

6. The inverse Radon approximation. As in [12] we consider the case of a single point source to motivate the inverse Radon approximation as a reconstruction scheme for arbitrary compactly supported sources. For a point source $f = \delta_{\boldsymbol{z}}$ located at $\boldsymbol{z} \in \mathbb{R}^3$ it follows from (4.1) and (4.2) that

$$\langle P_{\mathrm{i}\kappa}\delta_{\boldsymbol{z}}, h\rangle_{T^2} \;=\; \langle \delta_{\boldsymbol{z}}, P^*_{\mathrm{i}\kappa}h\rangle_{\mathbb{R}^3} \;=\; \overline{(P^*_{\mathrm{i}\kappa}h)(\boldsymbol{z})} \;=\; \int_{S^2} e^{\mathrm{i}\kappa\boldsymbol{\theta}\cdot\boldsymbol{z}}\overline{h(\boldsymbol{\theta},\boldsymbol{z}'_{\boldsymbol{\theta}})}\,\mathrm{d}s(\boldsymbol{\theta})\,,$$

i.e.,

$$(P_{\mathrm{i}\kappa}\delta_{\boldsymbol{z}})(\boldsymbol{\theta},\boldsymbol{p}) = e^{\mathrm{i}\kappa\boldsymbol{\theta}\cdot\boldsymbol{z}}\delta(\boldsymbol{p}-\boldsymbol{z}'_{\boldsymbol{\theta}})\,, \qquad \boldsymbol{\theta}\in S^2,\ \boldsymbol{p}\in\boldsymbol{\theta}^\perp\,. \tag{6.1}$$

Assuming that the second term on the right hand side of (5.1), respectively, (5.2), is small, it follows from the latter (with $\boldsymbol{\omega}$ replaced by $-\kappa\boldsymbol{p}$ with $\boldsymbol{p}\in\boldsymbol{\theta}^\perp$) and (4.5) that

$$(S_\varepsilon u^\infty)(-\boldsymbol{\theta},-\kappa\boldsymbol{p}) \;\approx\; \big(\psi_{\varepsilon\kappa} * (P_{\mathrm{i}\kappa}\delta_{\boldsymbol{z}})\big)(\boldsymbol{\theta},\boldsymbol{p}) \;=\; \sqrt{2\pi\varepsilon^2}\,e^{\mathrm{i}\kappa\boldsymbol{\theta}\cdot\boldsymbol{z}}e^{-\frac{1}{2}|\boldsymbol{p}-\boldsymbol{z}'_{\boldsymbol{\theta}}|^2\varepsilon^2\kappa^2}. \tag{6.2}$$

Therefore,

$$\begin{aligned}\big|(S_\varepsilon u^\infty)(-\boldsymbol{\theta},-\kappa\boldsymbol{p})\big| \;&\approx\; \sqrt{2\pi\varepsilon^2}\,e^{-\frac{1}{2}|\boldsymbol{p}-\boldsymbol{z}'_{\boldsymbol{\theta}}|^2\varepsilon^2\kappa^2}\\ &=\; e^{-1/(2\varepsilon^2)}\big(P(g_{\varepsilon\kappa}*\delta_{\boldsymbol{z}})\big)(\boldsymbol{\theta},\boldsymbol{p})\,,\end{aligned} \tag{6.3}$$

where $P : C_0^\infty(\mathbb{R}^3) \to C_0^\infty(T^2)$,

$$(Pg)(\boldsymbol{\theta},\boldsymbol{p}) \;=\; \int_{\mathbb{R}} g(\boldsymbol{p}+t\boldsymbol{\theta})\,\mathrm{d}t\,, \qquad \boldsymbol{\theta}\in S^2\,,\ \boldsymbol{p}\in\boldsymbol{\theta}^\perp\,,$$

denotes the standard ray transform (cf. [21, 22]).

We conclude from (6.3) that for a point source $f = \delta_{\boldsymbol{z}}$ the absolute values of the windowed Fourier transform of the far field pattern u^∞ yield—within our approximation error—the standard ray transform of a rescaled three-dimensional rotationally symmetric Gaussian centered at the source point $\boldsymbol{z}$. Note that we thus have data for the ray transform for all $\boldsymbol{\theta}\in S^2$ and all $\boldsymbol{p}\in\boldsymbol{\theta}^\perp$, which happens to be far more than what is actually needed to invert the ray transform (see section 8.4).

Due to linearity, (6.2) immediately carries over to arbitrary superpositions of point sources, say, e.g., $f = \alpha_1\delta_{\boldsymbol{z}_1} + \alpha_2\delta_{\boldsymbol{z}_2}$ with $\alpha_1,\alpha_2\in\mathbb{C}$, and $\boldsymbol{z}_1\neq\boldsymbol{z}_2$, but when taking absolute values in (6.3) this does result in interference effects. However, since the exponential on the right hand side of (6.2) decays rapidly away from $\boldsymbol{p} = \boldsymbol{z}'_{\boldsymbol{\theta}}$, these interferences are largely restricted to the area around intersections of the supports of $P\delta_{\boldsymbol{z}_1}$ and $P\delta_{\boldsymbol{z}_2}$. By virtue of (6.1) the support of $P\delta_{\boldsymbol{z}}$ is the graph of the function $\boldsymbol{\theta}\mapsto\boldsymbol{z}'_{\boldsymbol{\theta}}$; accordingly, the supports of $P\delta_{\boldsymbol{z}_1}$ and $P\delta_{\boldsymbol{z}_2}$ have only two points in common corresponding to $\boldsymbol{\theta} = \pm(\boldsymbol{z}_1-\boldsymbol{z}_2)/|\boldsymbol{z}_1-\boldsymbol{z}_2|\in S^2$ and $\boldsymbol{p} = \boldsymbol{z}_1{}'_{\boldsymbol{\theta}} = \boldsymbol{z}_2{}'_{\boldsymbol{\theta}}$. Since the data at hand are highly redundant, we expect that these minor interferences do not deteriorate the approximation (6.3) too much, as long as the sources are sufficiently well separated.

Developing this further, we may reinterpret arbitrary compactly supported sources as continua of point sources, and accordingly consider the absolute values of the windowed Fourier transform of the corresponding far field patterns as approximate ray transform data related to a mollified version of the source.

7. Numerical implementation and sampling. In this section we propose a numerical algorithm based on our findings from the previous sections to recover information on the support of the source f.

First we need to implement the windowed Fourier transform $(S_\varepsilon u^\infty)(\boldsymbol{\theta}, \boldsymbol{\omega})$ of (3.2) for certain $\boldsymbol{\theta} \in S^2$ and $\omega \in \boldsymbol{\theta}^\perp$. To this end we parameterize $\boldsymbol{\theta} \in S^2$ in the usual way, i.e.,

$$\boldsymbol{\theta} \,=\, \boldsymbol{\theta}(\vartheta, \varphi) \,=\, \begin{bmatrix} \sin\vartheta\cos\varphi \\ \sin\vartheta\sin\varphi \\ \cos\vartheta \end{bmatrix}, \qquad 0 \le \varphi < 2\pi\,,\ 0 \le \vartheta \le \pi\,,$$

and compute the windowed Fourier transform on $\boldsymbol{\theta}^\perp$ with a two-dimensional FFT over a square Cartesian grid with respect to the orthonormal basis $\{\boldsymbol{\sigma}, \boldsymbol{\tau}\}$ of $\boldsymbol{\theta}^\perp$ given by

$$\boldsymbol{\sigma} \,=\, \begin{bmatrix} -\sin\varphi \\ \cos\varphi \\ 0 \end{bmatrix} \qquad \text{and} \qquad \boldsymbol{\tau} \,=\, \begin{bmatrix} -\cos\vartheta\cos\varphi \\ -\cos\vartheta\sin\varphi \\ \sin\vartheta \end{bmatrix}.$$

Care has to be taken by choosing the mesh size h of the grid and the number K of grid points for the FFT algorithm. For fixed $\boldsymbol{\theta} \in S^2$ the windowed Fourier transform has been shown to approximate the exponential ray transform $(P_{\mathrm{i}\kappa}(g_{\varepsilon\kappa} * f))(-\boldsymbol{\theta}, -\boldsymbol{\omega}/\kappa)$ in Theorem 5.1, and thus, $(S_\varepsilon u^\infty)(\boldsymbol{\theta}, \boldsymbol{\omega})$ is essentially supported in

$$\left\{ \boldsymbol{\omega} \in \boldsymbol{\theta}^\perp \;\middle|\; |\boldsymbol{\omega}| \le \kappa \left(R + \frac{3}{\varepsilon\kappa} \right) \right\},$$

where we adopt the common rule of thumb that $3/\varepsilon\kappa$ is the radius of the essential support of the Gaussian $g_{\varepsilon\kappa}$. According to the standard Fourier theory of sampling (see, e.g., [22, pp. 65–67]) we thus require

$$h \,\lesssim\, \frac{\pi}{\kappa R + 3/\varepsilon}\,. \tag{7.1}$$

The number of grid points, K, on the other hand, must be so large that Kh is larger than the width 6ε of the essential support of the windowed far field that is to be Fourier transformed. This yields

$$K \,\ge\, \frac{6\varepsilon}{h} \,\gtrsim\, \frac{6}{\pi}\,(\varepsilon\kappa R + 3)\,. \tag{7.2}$$

To apply the FFT we have to evaluate the integrand of (3.2) which in turn requires the far field at the projected grid points, the latter depending on the respective argument $\boldsymbol{\theta}$. In general not all of these have been measured, but they can be computed with the spherical harmonics expansion (2.4). Note that the corresponding coefficients a_n^m satisfy

$$\begin{aligned} a_n^m \,&=\, \int_{S^2} u^\infty(\boldsymbol{\theta})\overline{Y_n^m(\boldsymbol{\theta})}\,\mathrm{d}s(\boldsymbol{\theta}) \\ &=\, \int_0^\pi \gamma_n^m P_n^{|m|}(\cos\vartheta) \int_0^{2\pi} e^{-\mathrm{i}m\varphi} u^\infty(\vartheta, \varphi)\,\mathrm{d}\varphi\,\sin\vartheta\,\mathrm{d}\vartheta \\ &=\, \int_{-1}^1 \gamma_n^m P_n^{|m|}(\mu) \left(\int_0^{2\pi} e^{-\mathrm{i}m\varphi} u^\infty(\arccos\mu, \varphi)\,\mathrm{d}\varphi \right) \mathrm{d}\mu\,, \end{aligned}$$

where $P_n^{|m|}$ are the associated Legendre functions and γ_n^m are suitable normalization constants; cf., e.g., [5, pp. 24–25]. Accordingly, these coefficients can be computed with a one-dimensional FFT in the φ variable and the Gauss–Legendre quadrature rule for the integral over the μ variable, provided that far field data are given at an equiangular grid for φ and those values $\vartheta_j = \arccos \mu_j$ corresponding to the Gaussian nodes μ_j. In view of the fact that the coefficients a_n^m are essentially zero for $n \gtrsim \kappa R$ (and hence, for $|m| \gtrsim \kappa R$) it is sufficient to sample the far field in φ direction with

$$M \gtrsim 2\kappa R \tag{7.3}$$

equidistant angles, and to use $N \gtrsim \kappa R$ Gaussian nodes in ϑ direction.

For each $\boldsymbol{\theta} \in S^2$ the Fourier integral only requires the evaluation of a decent number of far field samples, as the integrand of (3.2) is essentially zero for $|\boldsymbol{p}| > 3\varepsilon$. However, this amount of work is still time consuming. Alternatively, one therefore may consider a simple linear interpolation of the (given) measured data u^∞, in which case a more regular grid of measurement points may be appropriate. For example, following Driscoll and Healy [8, Thm. 3], it is appropriate under our conditions to sample the far field at M equidistant angles $\varphi \in [0, 2\pi)$ and the same number of equidistant angles $\vartheta \in [0, \pi]$, where M is again given by (7.3).

In this manner the windowed Fourier transform can be evaluated for any fixed $\boldsymbol{\theta} \in S^2$. In view of (6.3) and the discussion thereafter the absolute values of these numbers, our *meta data*, approximate a complete set of two-dimensional parallel projections

$$P(g_{\varepsilon\kappa} * f)(\boldsymbol{\theta}, \cdot) : \boldsymbol{\theta}^\perp \to \mathbb{C}^2$$

of the ray transform—up to a constant scaling factor $e^{-1/(2\varepsilon^2)}$.

Once these parallel projections have been computed for all $\boldsymbol{\theta} = \boldsymbol{\theta}(\vartheta, \varphi) \in S^2$ from an equiangular grid $(\vartheta, \varphi) \subset [0, \pi] \times [0, 2\pi)$ we apply in a second step a filtered backprojection algorithm implementing Orlov's inversion formula; cf., e.g., [22, pp. 20–21]. This then provides the searched for information about $g_{\varepsilon\kappa} * f$, and in particular about its support, respectively, the support of the given source f.

8. Numerical results. To illustrate our findings we present some numerical examples. Here we first concentrate on the special case of point sources, because in this case all steps in the reconstruction algorithm can be evaluated analytically (see section 6) and thus the performance of the algorithm for different wave numbers, noisy data, and limited aperture can be discussed more comprehensively. However, as pointed out in the introduction, our main interest is in the reconstruction of arbitrary compactly supported sources and in particular in inverse scattering with a single incident wave and not necessarily small scatterers. A corresponding example is discussed in section 8.5 below.

8.1. Point sources. We consider a collection of three point sources

$$f = \alpha_1 \delta_{z_1} + \alpha_2 \delta_{z_2} + \alpha_3 \delta_{z_3}$$

located at $z_1 = (0, 0, 2)$, $z_2 = (0, 3, 0)$, and $z_3 = (-3, -3, -3)$ with strengths $\alpha_1 = 1$, $\alpha_2 = 2\mathrm{i}$, and $\alpha_3 = 1 + \mathrm{i}$, respectively, as depicted in Figure 8.1 (left). For better visualization this plot shows small balls of radius 0.1 around the individual source points, and their projections on the three coordinate planes. For this example $R \approx 5.2$ is the radius of the smallest ball around the origin that contains all sources. We use

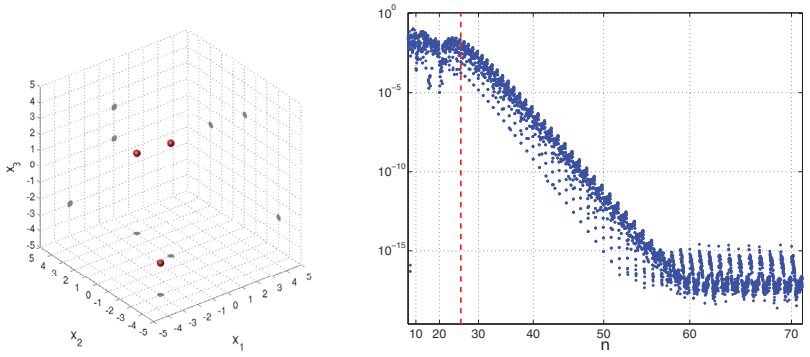

FIG. 8.1. *Left: Visualization of the three point sources. Right: Absolute values of the spherical harmonics coefficients of the corresponding far field pattern u^∞ for $\kappa = 5$.*

the wave number $\kappa = 5$, hence the individual source points are, roughly, three to six wave lengths apart.

The right-hand side plot in Figure 8.1 shows the absolute values $|a_n^m|$, $n = 0 \dots 70$, $m = -n, \dots, n$, of the spherical harmonics coefficients of the far field pattern u^∞ radiated by f, starting with $a_0^0; a_1^{-1}, a_1^0, a_1^1$; and so on. The plot exhibits the typical behavior of these coefficients as discussed in the previous section: There is a "low frequent" part, corresponding to indices $|n| \lesssim \kappa R \approx 26$, where the spherical harmonics coefficients are of comparable size. Then, starting at about $|n| \approx \kappa R$ as indicated by the dashed vertical line in the plot, the spherical harmonics coefficients decay linearly (or even superlinearly), in agreement with the corresponding behavior of the spherical Bessel functions (cf. (2.5) and (2.6)); this is the second ("high frequency") part. From the transient regime near the dashed line one can deduce a rough estimate of κR, and hence, R. Finally, for $n \gtrsim 55$ in this example, the plot of the spherical harmonics expansion exhibits a plateau at the level of (numerical or data) noise.

For the implementation of the inverse Radon approximation of the three source points we use simulated far field data at the equiangular grid

$$\boldsymbol{\Theta} := \left\{ \boldsymbol{\theta}(\vartheta_m, \varphi_n) \,\middle|\, \vartheta_m = m\pi/M,\ \varphi_n = 2n\pi/M,\ m, n = 0, \dots, M \right\} \tag{8.1}$$

on the unit sphere, where $M = 64$ in compliance with (7.3). Far field data in between these grid points are computed by linear interpolation. For the windowed Fourier transform we use the parameters

$$\varepsilon = \pi/10\,, \qquad h = \pi/50\,, \qquad \text{and} \qquad K = 32\,; \tag{8.2}$$

see section 7.

Figure 8.2 shows gray-scale plots of our meta data

$$\left|(S_\varepsilon u^\infty)(-\boldsymbol{\theta}, -\kappa \boldsymbol{p})\right| \approx e^{-1/(2\varepsilon^2)} \sum_{l=1}^{3} \big(P(g_{\varepsilon\kappa} * \delta_{\boldsymbol{z}_l})\big)(\boldsymbol{\theta}, \boldsymbol{p})\,, \qquad \boldsymbol{p} \in \boldsymbol{\theta}^\perp\,, \tag{8.3}$$

for the three directions $\boldsymbol{\theta} = \boldsymbol{e}_1$, $\boldsymbol{\theta} = \boldsymbol{e}_2$, and $\boldsymbol{\theta} = \boldsymbol{e}_3$ (left to right), respectively, where $\{\boldsymbol{e}_1, \boldsymbol{e}_2, \boldsymbol{e}_3\}$ denotes the standard Cartesian basis of $\mathbb{R}^3$. The axes of these plots have been rearranged for the reader's convenience to allow for a comparison with the projections onto the coordinate planes shown in Figure 8.1.

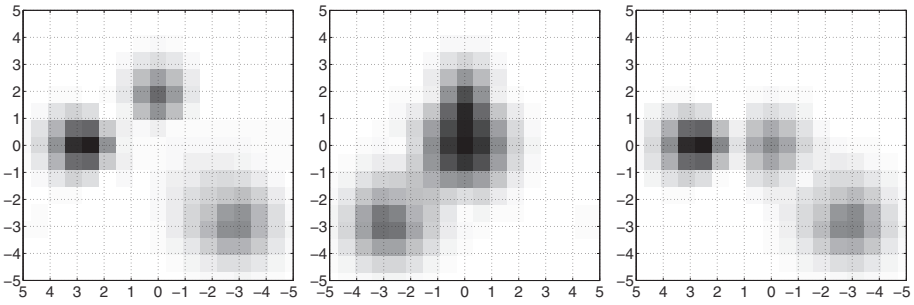

FIG. 8.2. *Approximations of parallel projections* $(P(g_{\varepsilon\kappa} * f))(\boldsymbol{\theta}, \cdot)$ *of the three point sources for* $\kappa = 5$ *(*$\varepsilon = \pi/10$*) for different directions* $\boldsymbol{\theta} \in S^2$*. Left:* $\boldsymbol{\theta} = \boldsymbol{e}_1$*. Middle:* $\boldsymbol{\theta} = \boldsymbol{e}_2$*. Right:* $\boldsymbol{\theta} = \boldsymbol{e}_3$*.*

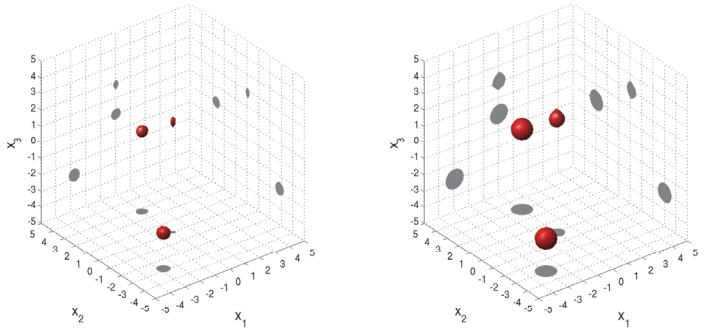

FIG. 8.3. *Left: Reconstruction of the three point sources for* $\kappa = 5$ *(*$\varepsilon = \pi/10$*). Right: Same as left, but using far field data containing* 50% *uniformly distributed additive noise and a smaller window (*$\varepsilon = \pi/20$*).*

For the inverse Radon reconstruction we apply the filtered backprojection algorithm for the ray transform to these meta data at $\boldsymbol{\theta} \in \boldsymbol{\Theta}$ and evaluate the resulting approximation, F, say, on a three-dimensional Cartesian grid with mesh width 0.2 in the region of interest $[-5, 5]^3$. From (8.3) we expect that the regions where F is nonnegligible are related to the support of the mollified version $g_{\varepsilon\kappa} * f$ of the unknown source.

Here and in the following examples the value $\varepsilon = \varepsilon(\kappa)$ has been optimized by means of numerical experiments for a single point source such that the corresponding meta data provide a sufficiently good approximation of parallel projections of a Gaussian blur with best possible resolution (see (6.3)). This numerical study suggests decreasing the standard deviation of the Gaussian window χ_ε like $1/\sqrt{\kappa}$ when increasing the wave number κ, which is in accordance with (5.1) and (6.3).

The value $K = 32$ in (8.2) has been chosen larger than actually required by (7.2) in order to be able to evaluate the filtered backprojection of the meta data on the whole cube $[-5, 5]^3$ and not just around the essential support of $g_{\varepsilon\kappa} * f$.

Figure 8.3 (left) shows isosurfaces of the resulting reconstruction F that can be used to localize the mollified source support. The individual levels of these isosurfaces differ and have to be chosen adaptively, as the proper choice depends on the distance to the origin and the individual strength of the respective source component. Here we have used the following ad hoc procedure: First we determine the positions of all

local maxima $\boldsymbol{y}_l \in (-5,5)^3$ of F, discarding those that are less than four pixels apart, or for which $|F(\boldsymbol{y}_l)| < 0.1 \max|F|$; removing local maxima of small value turns out to be particularly important at higher wave numbers. Then, for each local maximum we set

$$F_l \;=\; 0.9\,|F(\boldsymbol{y}_l)| \tag{8.4}$$

to be the level of the corresponding (local) isosurface. As can be seen these reconstructions agree very well with the true positions of the point sources shown in Figure 8.1.

8.2. Point sources and noisy data. For a second test case we add 50% uniformly distributed noise to the previous far field data to study the sensitivity of the method with respect to noise. As already pointed out in [12] for the two-dimensional case, it is useful to decrease the window size ε in the presence of noise to increase the amount of smoothing in the reconstruction, as this has a regularizing effect. Accordingly, we choose

$$\varepsilon \;=\; \pi/20\,, \qquad h \;=\; \pi/50\,, \qquad \text{and} \qquad K \;=\; 32\,.$$

Despite the huge amount of noise the corresponding reconstruction shown in Figure 8.3 (right) is still satisfactory, although the corresponding parallel projections are severely distorted already (see Figure 8.4). One reason for this is the large number of roughly $M^2 = 64^2$ measurement data used by the algorithm and the fact that the meta data $|S_\varepsilon u^\infty|$ are actually strongly redundant (see section 8.4 below).

8.3. Smaller and larger wave numbers. For the same geometry, but smaller wave number $\kappa = 2$, we can choose our parameters as $M = 32$, as well as

$$\varepsilon \;=\; \pi/6\,, \qquad h \;=\; \pi/20\,, \qquad \text{and} \qquad K \;=\; 32\,.$$

A gray-scale plot of the corresponding parallel projection $|(S_\varepsilon u^\infty)(-\boldsymbol{\theta}, -\kappa\boldsymbol{p})|$ for $\boldsymbol{\theta} = \boldsymbol{e}_3$ is shown in Figure 8.5 (left). As expected, the resolution is much worse than in Figure 8.2. Similar results are shown for $\kappa = 10$ in Figure 8.5 (middle), where $M = 128$,

$$\varepsilon \;=\; \pi/15\,, \qquad h \;=\; \pi/100\,, \qquad \text{and} \qquad K \;=\; 64\,,$$

and for $\kappa = 20$ in Figure 8.5 (right), where $M = 256$ with

$$\varepsilon \;=\; \pi/20\,, \qquad h \;=\; \pi/200\,, \qquad \text{and} \qquad K \;=\; 64\,.$$

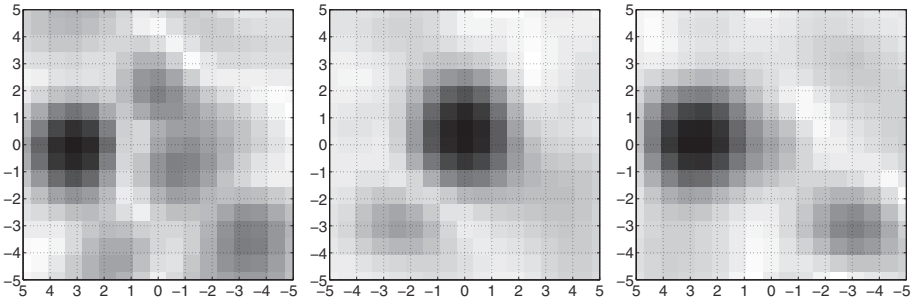

FIG. 8.4. *Same as Figure* 8.2*, but using far field data containing* 50% *uniformly distributed additive noise and a smaller window* ($\varepsilon = \pi/20$).

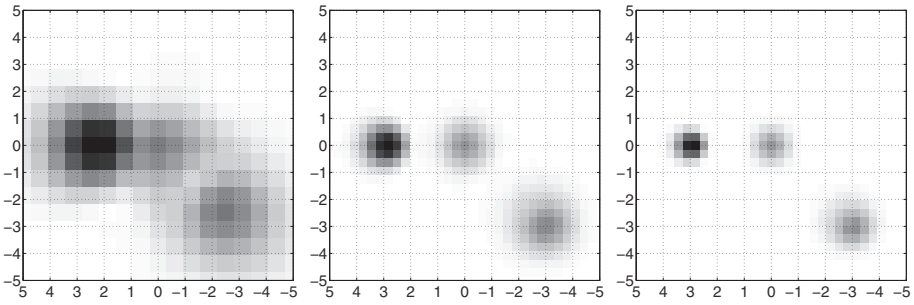

FIG. 8.5. *Same as in Figure* 8.2 *(right), but now with varying* κ *and* ε. *Left:* $\kappa = 2$, $\varepsilon = \pi/6$. *Middle:* $\kappa = 10$, $\varepsilon = \pi/15$. *Right:* $\kappa = 20$, $\varepsilon = \pi/20$.

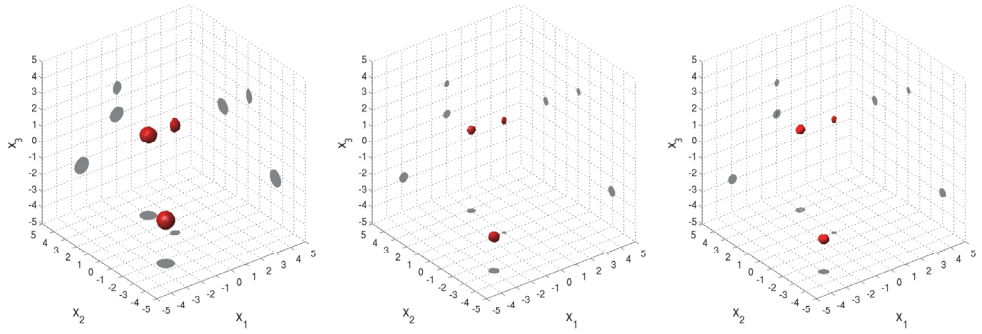

FIG. 8.6. *Same as in Figure* 8.3 *(left), but now with varying* κ *and* ε. *Left:* $\kappa = 2$, $\varepsilon = \pi/6$. *Middle:* $\kappa = 10$, $\varepsilon = \pi/15$. *Right:* $\kappa = 20$, $\varepsilon = \pi/20$.

The corresponding isosurface plots can be found in Figure 8.6. Here we use the same threshold factor as in (8.4) except for $\kappa = 20$, where we change this factor to 0.8 since otherwise the isosurfaces would be very small.

For wave numbers smaller than $\kappa = 2$ the method fails since the reconstruction F becomes very smooth and not all sources appear as local maxima of F anymore. With increasing wave number the numerical computations become more time consuming due to the need to fulfill the sampling conditions (7.1), (7.2), and (7.3).

8.4. Limited aperture. The fact that Orlov's inversion formula for the inverse ray transform applies to limited view data, cf. [22, p. 18–21], where $\boldsymbol{\theta}$ varies on a spherical zone

$$S_0^2 = \{\boldsymbol{\theta}(\vartheta, \varphi) \mid -\vartheta_0 \le \vartheta \le \vartheta_0\,,\ 0 \le \varphi < \varphi_0\}$$

with some $\vartheta_0 > 0$ and $\varphi_0 \ge \pi$, allows us to extend our method to the case where far field samples are only given on such a subset of S^2. As the windowed Fourier transform (3.2) of the far field data requires projections of $\boldsymbol{\theta} + \boldsymbol{p}$, $\boldsymbol{p} \in \boldsymbol{\theta}^\perp$, onto S_0^2 for $|\boldsymbol{p}| < 3\varepsilon$, our meta data can then be computed for

$$\boldsymbol{\theta} \in \widetilde{S}_0^2 = \{\boldsymbol{\theta}(\vartheta, \varphi) \mid -\vartheta_0 + \tilde{\varepsilon} \le \vartheta \le \vartheta_0 - \tilde{\varepsilon}\,,\ \tilde{\varepsilon} \le \varphi < \varphi_0 - \tilde{\varepsilon}\},$$

where $\tilde{\varepsilon} = \arcsin(3\varepsilon)$, and $\vartheta_0 - \tilde{\varepsilon}$ must still be positive.

S_0^2 and $\widetilde{S}_0^2$ are illustrated in the left-hand side plot of Figure 8.7; this is a true to scale plot for $\vartheta_0 = \pi/6$, $\varphi_0 = \pi$, and parameter $\varepsilon = \pi/20$. Accordingly, $2(\vartheta_0 - \tilde{\varepsilon}) \approx$

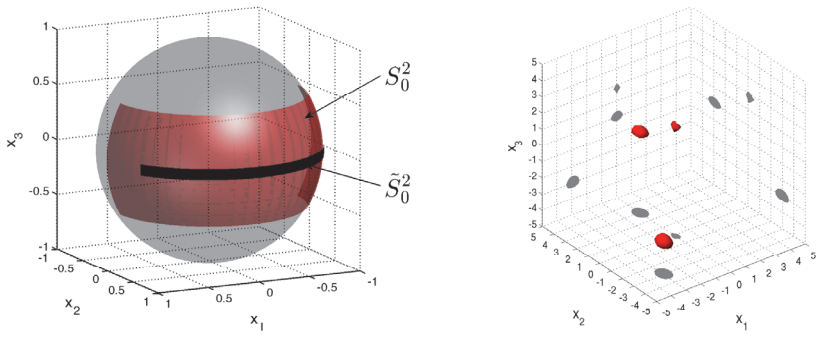

FIG. 8.7. *Left: Illustration of the spherical zones S_0^2 and $\widetilde{S}_0^2$. Right: Same as Figure* 8.3 *(left), but using limited aperture data on S_0^2 ($\varepsilon = \pi/20$).*

3.8° is the latitude variation of $\widetilde{S}_0^2$. Considering the restriction of the far field data used in section 8.1 to this S_0^2 we recompute the same example as before with wave number $\kappa = 5$. Aside from the smaller value of ε, which we decrease to increase the size of $\widetilde{S}_0^2$ accordingly, we use the same parameters as in (8.2), i.e.,

$$h = \pi/50\,, \qquad K = 32\,, \qquad \text{and} \qquad M = 64.$$

Note that this only yields the windowed Fourier transform of the far field pattern on 3×51 points $\boldsymbol{\theta}$.

Figure 8.7 (right) shows the corresponding isosurface plot of the reconstruction. The results are still satisfactory.

8.5. Inverse scattering. In our final but most important example we apply the reconstruction algorithm from section 7 to far field data corresponding to an obstacle scattering problem. We consider an incident plane wave $u^i(\boldsymbol{x}) = e^{\mathrm{i}\kappa \boldsymbol{x}\cdot\boldsymbol{d}}$, $\boldsymbol{x} \in \mathbb{R}^3$, with direction of propagation $\boldsymbol{d} = \boldsymbol{e}_1$ and wave number $\kappa = 5$ that is scattered by the two impenetrable objects shown in Figure 8.8 (left). The diameters of these scatterers amount to 1.6 and 2.5 wave lengths, respectively, so that they certainly cannot be considered point-like. Furthermore, these obstacles are taken to have different physical properties; while the ellipsoid is sound soft, the torus is sound hard. Accordingly, the scattered field u^s satisfies the homogeneous Helmholtz equation together with the Sommerfeld radiation condition away from the obstacles with homogeneous Dirichlet, respectively, Neumann boundary conditions at their boundaries. The scattered field can be written as a volume potential as in (2.1) with a smooth density f supported in an arbitrarily small neighborhood of the obstacles.

Although f consists now of continuous superpositions of point sources, our reconstruction method is still applicable and yields useful information about the number and the positions of the two scatterers. To demonstrate this, we simulate the far field pattern of the scattered field on the equiangular grid $\boldsymbol{\Theta} \subset S^2$ from (8.1) with $M = 128$ using a boundary element method.[1] We compute the windowed Fourier transform of the far field pattern using the parameters

$$\varepsilon = \pi/10\,, \qquad h = \pi/100\,, \qquad \text{and} \qquad K = 64\,,$$

[1]The data have been generated using the C++ boundary element library BEM++ (see Śmigaj et al. [24]).

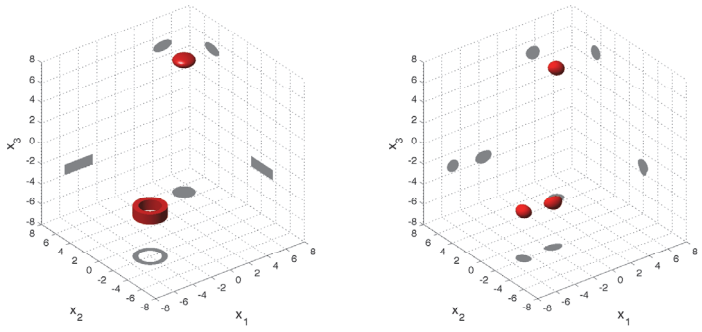

FIG. 8.8. *Left: Visualization of the geometry of the scatterers. Right: Reconstruction of the two scatterers for* $\kappa = 5$ *(*$\varepsilon = \pi/10$*).*

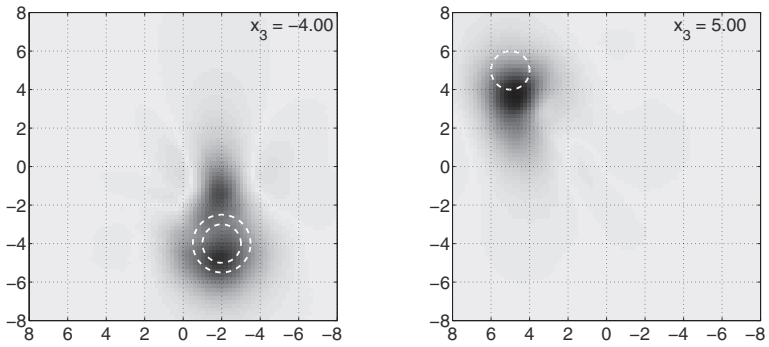

FIG. 8.9. *Horizontal cross-sections of the reconstruction* F *in the region of interest for different for different values of* x_3*. Left:* $x_3 = -4$*. Right:* $x_3 = 5$*.*

take absolute values and evaluate the filtered backprojection on a three-dimensional Cartesian grid with mesh width 0.2 in the region of interest, i.e., in $[-8, 8]^3$. Note that this interval is somewhat larger than in the previous examples, hence the increased values of the parameters K, M, and $1/h$; cf. (7.1)–(7.3).

Figure 8.8 (right) shows the isosurface plot of the reconstruction, where we use 0.8 as threshold factor in (8.4); horizontal cross-sectional plots of the reconstruction F in the region of interest at height $x_3 = -4$ and $x_3 = 5$ can be found in Figure 8.9. Here we included the true scatterer geometries as white dashed lines. The absence of oscillatory artifacts in these plots is an attraction of our scheme when compared, e.g., to regularized least squares methods or backpropagation algorithms. While the ellipsoid is recovered reasonably well, the method yields two separated objects instead of a torus. This is due to the strong reflections of the incident wave at the corresponding boundary faces of the torus.

9. Conclusions. We have shown that a windowed Fourier transform of the far field pattern radiated by a compactly supported source is an approximation of an exponential ray transform with purely imaginary exponent of this source. Up to certain interferences a filtered backprojection for the standard ray transform applied to the absolute values of this windowed Fourier transform yields information on the

support of the source, such as the number and the positions of well separated source components. This knowledge can subsequently be used as initial guess for other inversion schemes to further enhance the reconstruction.

We have described an implementation of this scheme, and we have presented numerical tests which confirm that the method works better at higher frequencies; in particular the resolution of the reconstructions improves with increasing wave number. In this case, on the other hand, the computational complexity of the algorithm increases, too, due to the need to sample the far field data and its windowed Fourier transform on finer grids. An advantage of the scheme is the absence of oscillatory artifacts in the reconstructions. We also have exemplified that the method extends well to limited aperture data, as long as the aperture covers a sufficiently large spherical zone.

The main application we have in mind is single frequency inverse scattering with a single incident wave and no a priori knowledge on physical and topological properties of the scatterers, an instance for which only few reasonable reconstruction methods are known. We have shown that our method can be applied to such problems and that the quality of the reconstruction depends on the distribution of the virtual sources of the scattered field on the boundary of the scatterers.

Acknowledgments. The authors wish to thank Prof. Peter Monk for his help in simulating the forward data for the final example in section 8.5.

REFERENCES

[1] M. Abramowitz and I. A. Stegun, *Handbook of Mathematical Functions, with Formulas, Graphs, and Mathematical Tables*, Dover Publications, New York, 1966.
[2] C. Alves, R. Kress, and P. Serranho, *Iterative and range test methods for an inverse source problem for acoustic waves*, Inverse Problems, 25 (2009), 055005.
[3] G. Bellizzi and A. Capozzoli, *Estimation of the support of a radiating/scattering object by means of supporting cones*, Inverse Problems, 27 (2011), 035001.
[4] A. Chai, M. Moscoso, and G. Papanicolaou, *Robust imaging of localized scatterers using the singular value decomposition and ℓ^1 minimization*, Inverse Problems, 29 (2013), 025016.
[5] D. Colton and R. Kress, *Inverse Acoustic and Electromagnetic Scattering Theory*, 2nd ed., Springer, Berlin, 1998.
[6] A.J. Devaney, *Mathematical Foundations of Imaging, Tomography and Wavefield Inversion*, Cambridge University Press, Cambridge, 2012.
[7] A.J. Devaney, E.A. Marengo, and M. Li, *Inverse source problem in nonhomoegeneous background media*, SIAM J. Appl. Math., 67 (2007), pp. 1353–1378.
[8] J. R. Driscoll and D. M. Healy, Jr., *Computing Fourier transforms and convolutions on the 2-sphere*, Adv. Appl. Math., 15 (1994), pp. 202–250.
[9] A. El Badia and T. Nara, *An inverse source problem for Helmholtz's equation from the Cauchy data with a single wave number*, Inverse Problems, 27 (2011), 105001.
[10] A.C. Fannjiang, T. Strohmer, and P. Yan, *Compressed remote sensing of sparse objects*, SIAM J. Imaging Sci., 3 (2010), pp. 595–618.
[11] I.S. Gradshteyn and I.M. Ryzhik, *Table of Integrals, Series, and Products*, 7th ed., Academic Press, New York, 2007.
[12] R. Griesmaier, M. Hanke, and T. Raasch, *Inverse source problems for the Helmholtz equation and the windowed Fourier transfrom*, SIAM J. Sci. Comput., 34 (2012), pp. A1544-A1562.
[13] R. Griesmaier, M. Hanke, and J. Sylvester, *Far field splitting for the Helmholtz equation*, submitted.
[14] M. Hanke, *One shot inverse scattering via rational approximation*, SIAM J. Imaging Sci., 5 (2012), pp. 465–482.
[15] S. Helgason, *The Radon Transform*, Birkhäuser, Boston, 1980.
[16] M. Ikehata, *Reconstruction of a source domain from the Cauchy data*, Inverse Problems, 15 (1999), pp. 637–645.
[17] V. Isakov, *Inverse Source Problems*, AMS, Providence, RI, 1990.

[18] R. Kress and W. Rundell, *Reconstruction of extended sources for the Helmholtz equation*, Inverse Problems, 29 (2013), 035005.
[19] S. Kusiak and J. Sylvester, *The scattering support*, Comm. Pure Appl. Math., 56 (2003), pp. 1525–1548.
[20] S. Kusiak and J. Sylvester, *The convex scattering support in a background medium*, SIAM J. Math Anal., 36 (2005), pp. 1142–1158.
[21] F. Natterer, *The Mathematics of Computerized Tomography*, Teubner/Wiley, New York, 1986.
[22] F. Natterer and F. Wübbeling, *Mathematical Methods in Image Reconstruction*, SIAM, Philadelphia, 2001.
[23] R. Potthast, J. Sylvester, and S. Kusiak, *A "range test" for determining scatterers with unknown physical properties*, Inverse Problems, 19 (2003), pp. 533–547.
[24] W. Śmigaj, S. Arridge, T. Betcke, J. Phillips, and M. Schweiger, *Solving Boundary Integral Problems with BEM++*, preprint.
[25] J. Sylvester, *Notions of support for far fields*, Inverse Problems, 22 (2006), pp. 1273–1288.
[26] B. Torresani, *Position-frequency analysis for signals defined on spheres*, Signal Processing, 43 (1995), pp. 341–346.